PAPER • OPEN ACCESS

Slice NEQ and system DQE to assess CT imaging performance

View the article online for updates and enhancements.

Physics in Medicine & Biology

IPEM Institute of Physics and Engineering in Medicine

PAPER

Slice NEQ and system DQE to assess CT imaging performance

P Monnin[1], A Viry, F R Verdun and D Racine

Institute of Radiation Physics (IRA), Lausanne University Hospital (CHUV) and University of Lausanne, Rue du Grand-Pré 1, 1007 Lausanne, Switzerland

[1] Author to whom any correspondence should be addressed.

E-mail: pascal.monnin@chuv.ch

Abstract

The standard Fourier metrics used for assessing image quality in computed tomography (CT) use a planar (2D) formulation of the noise equivalent quanta (NEQ) without a specific concept to manage the influence of longitudinal resolution variations, thus create a bias in the comparison of image quality for different reconstructed slice thicknesses. For this work, we designed a 'slice NEQ' that takes the longitudinal resolution into account and provides a volumetric indication of the scanner imaging performance. We also developed a specific formulation for the system DQE at the CT isocentre. A cylindrical water phantom with three different inserts for three contrast levels (-100, 120 and 1000 HU) was used for the task-based transfer functions (TTF) and noise power spectra (NPS) measurements. The longitudinal TTF was measured using the point source of the Catphan® 600 phantom. Images of the phantoms were acquired on two scanners (GE Discovery 750 HD and Siemens SOMATOM Force) and reconstructed using different slice thicknesses between 1 and 5 mm and algorithms (FBP for both systems, ASIR 50 and ASIR-V 50 for the GE). The slice NEQ correctly compared the imaging performance for different longitudinal resolutions whereas the 2D NEQ increased proportionally with the reconstructed slice thickness. The system DQE peaked at 0.70 (at 0.1 mm^{-1}) for the Siemens and at 0.50 (at 0.1 mm^{-1}) for the GE for FBP reconstructions. The validity of these Fourier-based metrics was restricted to a limited range of contrast due to nonlinearities introduced when dealing with iterative reconstructions (IR).

1. Introduction

The concepts of noise equivalent quanta (NEQ) and detective quantum efficiency (DQE) for image quality and system characterization are standardized metrics in projection radiography (ICRU Report 54). They provide a basis for evaluating imaging performance in the frequency (Fourier) domain with respect to an air kerma level. For projection imaging, the NEQ is a key attribute that can be interpreted as a signal-to-noise ratio squared (SNR^2) and the DQE shows how an imaging system transfers the SNR^2 to the output image (Wagner and Brown 1985). These metrics have also been extended to computed tomography (CT) and cone-beam CT (CBCT), however their meaning is less obvious than in projection imaging. The filtered back projection (FBP) used for image reconstruction decouples the signal and noise transfer. Consequently, the NEQ for CT and CBCT does not represent a SNR^2 parameter like in projection imaging, but the number of photons an ideal detector would need to produce the same noise power spectrum (NPS). Hanson (1979) initially defined a scalar NEQ in terms of the number of photons contributing to the reconstructed slice per unit length of the detector, related to the low-frequency slope of the NPS (Wagner *et al* 1979, Faulkner and Moores 1984). Siewerdsen and Jaffray (2003) extended the concept to three-dimensional NEQ and DQE described in the frequency space for volume CT systems. 3D NEQ and DQE have been used in performance evaluation of various CT and CBCT systems and in mathematical model observers for task-based image quality assessment (Tward *et al* 2008, Tward and Siewerdsen 2008, Gang *et al* 2011, Tang *et al* 2012).

The 3D NEQ gives an exhaustive formulation for the volumetric reconstruction expressed in photons/mm^2, however it does not represent the in-plane image quality as observable on a reconstructed

slice. Hence, the planar (2D) formulation of the NEQ has been used for assessing in-plane image quality for CT, giving an effective number of photons per unit length of detector, expressed in photons/mm (Boedeker *et al* 2007, Tang *et al* 2012). The 2D NEQ ignores the effect of the longitudinal resolution on the signal, whereas the NPS measured on the images integrates the noise over the slice thickness. Therefore, a decrease in longitudinal resolution reduces the correlation between neighbouring pixels and decreases the noise in the slice without changing the in-plane MTF. This behaviour introduces a bias that makes the 2D NEQ practically proportional to the slice thickness for CT or CBCT. Hence, the 2D NEQ incorrectly compares the imaging performance for different slice thicknesses or different longitudinal resolutions.

The DQE is a figure of merit that gives the fraction of the incident number of photons that a perfect imaging system would need in order to produce the NEQ observed in the image. Despite the relevance of the DQE, the air kerma at the detector entrance is difficult to estimate for CT systems because the bowtie filter introduces a spatial dose variation (Hanson 1979, Wagner *et al* 1979). Furthermore, corrections for beam hardening or scatter applied during the reconstruction consider an object in the field of view. The assessment of CT imaging performance in air is intractable and needs an object. Instead of the DQE defined in air, we assessed a 'system DQE' by imaging a phantom that mimics patient attenuation together with beam hardening phenomena and scatter production. The calculation is then done using reconstructed images in which all data corrections have been applied.

Nonlinear iterative reconstruction (IR) are now widely used to improve CT image quality and reduce patient dose (Willemink *et al* 2013). Nonlinearities can lead to a contrast and dose dependent signal transfer that needs the use of task-based metrics to assess image quality. The works of Vaishnav *et al* (2014), Verdun *et al* (2015) and Samei *et al* (2019) give an overall overview of the methods recently developed for the performance evaluation of CT and CBCT systems using a task-based approach and describe their application to a number of tests for quality controls. The methods include spatial resolution assessment, noise analysis, and estimation of detectability using model observers in Fourier or spatial domain, but global image quality metrics such as NEQ and DQE are not addressed.

In this work, we present a task-based and unbiased formulation of in-plane NEQ for CT or CBCT images, named 'slice NEQ'. Based on the approximation of a spatially invariant imaging system considered linear in a small-contrast approximation, we calculated slice NEQs for two CT systems using measurements of in-plane TTF, longitudinal TTF and NPS on images acquired with different conditions. These metrics were developed to assess imaging performance for the basic (linear) FBP reconstruction. We have then tried to apply it using task-based transfer functions on images reconstructed with IR but the concept needs new developments to overcome the intrinsic limitations of metrics developed in the Fourier domain. An adaptation of the system DQE presented in recent work (Monnin *et al* 2017) was developed from the slice NEQ for evaluating the imaging efficiency of CT or CBCT systems using a cylindrical homogeneous phantom made of water or Plexiglas. The system DQE needed additional measurements of $CTDI_{air}$ and scatter fraction at the system input. We thus evaluated these metrics using measurements made on two CT systems with different doses, slices thicknesses and reconstruction kernels/algorithms.

2. Theory

We consider an imaging system to be composed of an anti-scatter device, a detector, and a reconstruction algorithm. The slice NEQ and system DQE presented below use resolution, noise, and dose measured at the system isocentre, within the limits of a locally homogeneous central x-ray field approximation. The first and second order image statistics are assumed to be locally homogeneous and shift invariant in the region of the centre of the reconstructed image (isocentre). Log-transformation of detector signal, iterative algorithms, and image processing used in tomographic reconstruction are nonlinear processes. The imaging systems are therefore considered linear only for a small range of signal variations within the images (small contrasts). The log-normalization used in FBP can be taken as a gain stage for this condition of small-signal approximation (Tward *et al* 2008). The experimental measurements must consequently be performed in a manner that follows such approximations, in particular the use of a small-signal approach to the TTF measurement. Homogeneous cylindrical phantoms (water or Plexiglas) containing low-contrast objects are typically used to produce images with small signal variations in a relatively homogeneous background.

2.1. Slice NEQ
The 3D NEQ for CT and CBCT systems given in equation (1) was adapted from equation (10) in Gang *et al* (2014).

$$NEQ_{3D}\left(f_x, f_y, f_z\right) = \pi \cdot \left(\frac{1000}{\mu_w}\right)^2 \cdot \sqrt{f_x^2 + f_y^2} \cdot \frac{TTF^2\left(f_x, f_y, f_z\right)}{NPS\left(f_x, f_y, f_z\right)} \tag{1}$$

The 3D NPS, expressed in HU^2 mm^3, is usually measured in a homogeneous region of interest (ROI) of water on the images. Compared to Gang *et al* (2014), the NPS is multiplied by the contrast scaling factor $(\mu_w/1000)^2$ that rescales HU values into values of linear attenuation of water μ_w (in mm^{-1}) for the effective beam energy calculated from the spectrum of the x-ray beam (Wagner *et al* 1979). The second difference compared to Gang *et al* (2014) is the use of the task-based transfer function (TTF) for the transfer function of the signal. The TTF is a contrast-dependent modulation transfer function (MTF) that helps characterise the resolution when dealing with nonlinear reconstruction algorithms for which image contrast influences the spatial resolution (Verdun *et al* 2015). The 3D TTF is the modulus of the Fourier transform of the 3D point spread function, and describes the 3D-resolution of the reconstructed volume. The 3D NEQ, expressed in photons/mm^2, represents the number of quanta per mm^2 that a perfect CT system would use to give the NPS observed in the slice.

The 3D NEQ gives an exhaustive formulation for the volumetric reconstruction, however it does not represent the in-plane image quality as observable on a reconstructed slice. Consequently, in-plane (2D) formulation of the NEQ has been used for assessing image quality for CT slices. In general, the NEQ for CT slices is calculated without considering the slice thickness, restricted to a 2D metric given in equation (2) (Boedeker *et al* 2007, Tang *et al* 2012).

$$NEQ_{2D}\left(f_x, f_y\right) = \pi \cdot \left(\frac{1000}{\mu_w}\right)^2 \cdot \sqrt{f_x^2 + f_y^2} \cdot \frac{TTF^2\left(f_x, f_y\right)}{NPS\left(f_x, f_y\right)} \tag{2}$$

The in-plane 2D NPS can be measured in slices of the reconstructed volume, however a synthetized 2D NPS obtained by integrating the 3D NPS over the longitudinal z-frequency bandwidth (equation (3)) is more accurate for imaging systems with limited spatial stationarity in the reconstructed volume (e.g. CBCT or helical scans) (Siewerdsen *et al* 2002). The in-plane 2D NPS is expressed in HU^2 mm^2.

$$NPS\left(f_x, f_y\right) = \int_{-\infty}^{\infty} NPS\left(f_x, f_y, f_z\right) df_z \tag{3}$$

The TTF is calculated in the reconstructed xy-plane regardless of the z-resolution (Richard *et al* 2012, Brunner and Kyprianou 2013). The 2D NEQ, expressed in photons/mm, represents the number of quanta per unit length of projection (for all the projections) that a perfect CT system would need to produce the NPS observed in the slice, no matter the reconstructed slice thickness. This leads to a situation where the 2D NEQ increases with the slice thickness, regardless the longitudinal imaging performance.

In order to consider the effect of longitudinal resolution on the correlation between pixels in the reconstructed image, we introduce a NEQ for a single slice, named 'slice NEQ'. The slice NEQ integrates both signal and noise powers over the slice thickness, namely the 3D TTF^2 and NPS over the z-frequency bandwidth of a slice (equation (4a)).

$$NEQ_{slice}\left(f_x, f_y\right) = \pi \cdot \left(\frac{1000}{\mu_w}\right)^2 \cdot \sqrt{f_x^2 + f_y^2} \cdot \frac{\int_{-\infty}^{\infty} TTF^2\left(f_x, f_y, f_z\right) df_z}{\int_{-\infty}^{\infty} NPS\left(f_x, f_y, f_z\right) df_z} \tag{4a}$$

The slice NEQ represents the number of photons per mm^2 that a perfect CT system would need in order to give the NPS observed in the slice, taking into account the reconstructed slice thickness. It is assumed that the spatial resolution in the image xy-plane and along the z-axis are resolved by different physical and reconstruction processes, and are separable, with $TTF\left(f_x, f_y, f_z\right) = TTF_{xy}\left(f_x, f_y\right) \cdot TTF_z\left(f_z\right)$. Separability between TTF_{xy} and TTF_z can be tested by ensuring that TTF_{xy} remains constant under varying axial resolutions (e.g. slice thicknesses), or that TTF_z does not change under varying in-plane resolutions (e.g. reconstruction kernels). Under this assumption, TTF_{xy} and TTF_z can be measured independently, and the slice NEQ can be calculated using equation (4b).

$$NEQ_{slice}\left(f_x, f_y\right) = \pi \cdot \left(\frac{1000}{\mu_w}\right)^2 \cdot \sqrt{f_x^2 + f_y^2} \cdot \frac{TTF_{xy}^2\left(f_x, f_y\right) \cdot \int_{-\infty}^{\infty} TTF_z^2\left(f_z\right) df_z}{\int_{-\infty}^{\infty} NPS\left(f_x, f_y, f_z\right) df_z} \tag{4b}$$

One way for accounting for the difference between the 2D and slice NEQ is to compare these two metrics for a system with a perfect longitudinal resolution.

2.1.1. Special case: perfect longitudinal resolution.

We consider here a set of CT slices with a slice thickness T_z and a slice interval Δz. A perfect z-resolution gives a pre-sampling TTF_z determined by the slice thickness T_z.

$$TTF_z\left(f_z\right) = \text{sinc}\left(\pi \cdot T_z \cdot f_z\right) \tag{5}$$

The integral of TTF_z^2 is approximately equal to $1/T_z$ for the range of slice thicknesses used in CT (between 0.5 and 10 mm).

$$\int_{-\infty}^{\infty} TTF_z^2 (f_z) \, df_z = \int_{-\infty}^{\infty} \text{sinc}^2 (\pi \cdot T_z \cdot f_z) \, df_z \cong \frac{1}{T_z} \tag{6}$$

The NPS sampled along the *z*-frequency axis is white in the *z*-frequency axis (equation (7)).

$$NPS (f_x, f_y, f_z) = NPS_{xy} (f_x, f_y) \cdot \sum_{k_z = -\infty}^{\infty} \text{sinc}^2 \left(\pi \cdot T_z \cdot \left(f_z - \frac{k_z}{\Delta z} \right) \right) = NPS_{xy} (f_x, f_y) \cdot \frac{\Delta z}{T_z} \tag{7}$$

The integral of the NPS over the *z*-frequency bandwidth determined by the Nyquist frequency $f_{z,Nyq} = 1/(2 \cdot \Delta z)$ is inversely proportional to the slice thickness.

$$\int_{-\infty}^{\infty} NPS (f_x, f_y, f_z) \, df_z = NPS_{xy} (f_x, f_y) \cdot \int_{-\infty}^{\infty} \frac{\Delta z}{T_z} df_z$$
$$= NPS_{xy} (f_x, f_y) \cdot \frac{\Delta z}{T_z} \cdot 2 f_{z,Nyq} = NPS_{xy} (f_x, f_y) \cdot \frac{1}{T_z} \tag{8}$$

Inserting equations (6) and (8) into equation (4*b*) shows the slice NEQ is independent of the slice thickness and sampling interval for a system with a perfect longitudinal resolution. For a real system with non-perfect longitudinal performance, the slice NEQ will decrease in proportion to the decorrelation between NPS_z and TTF_z^2.

2.2. System DQE

The photon fluence per unit air kerma φ (photons mm^{-2} µGy^{-1}) at the system (anti-scatter device + detector) entrance has no spatial correlation and is white. It is composed of primary (P_{in}) and scattered (S_{in}) photons that give an input air kerma $S_{in} + P_{in}$ (µGy) with an input scatter fraction $SF_{in} = S_{in}/(S_{in} + P_{in})$. The input NEQ, noted NEQ_{in}, has a constant amplitude, given by equation (9) (Monnin *et al* 2017).

$$NEQ_{in} = \varphi (P_{in} + S_{in}) (1 - SF_{in})^2 = \varphi P_{in} (1 - SF_{in}) \tag{9}$$

The system DQE (DQE_{sys}) for a CT slice is the ratio between the slice NEQ (equation (4*b*)) and NEQ_{in}.

$$DQE_{sys} (f_x, f_y) = \left(\frac{1000}{\mu_w} \right)^2 \cdot \frac{\pi \cdot \sqrt{f_x^2 + f_y^2} \cdot TTF_{xy}^2 (f_x, f_y) \cdot \int_{-\infty}^{\infty} TTF_z^2 (f_z) \, df_z}{\varphi \cdot P_{in} \cdot (1 - SF_{in}) \cdot \int_{-\infty}^{\infty} NPS (f_x, f_y, f_z) \, df_z} \tag{10}$$

If we consider a locally homogeneous x-ray fluence at the system input, P_{in} at the isocentre can be estimated from the CTDI$_{air}$ measured at the isocentre of the system, corrected for the attenuation of the cylindrical water phantom (diameter *d*) used for *TTF* and *NPS* measurements (at the isocentre), and for the distance (equation(11)).

$$P_{in} = CTDI_{air} \cdot \exp (-\mu_w d) \cdot \left(\frac{SID}{SDD} \right)^2 \tag{11}$$

Where *SID* and *SDD* are the source-to-isocentre (DICOM tag 0018,1111) and source-to-detector (DICOM tag 0018,1110) distances, respectively.

3. Material and methods

3.1. Data acquisition

Two CT systems were involved in this study: a GE Discovery 750 HD (GE Healthcare, Milwaukee, MI) and a Siemens SOMATOM Force (Siemens Healthcare, Forchheim, Germany). All scans used the helical mode with a pitch the closest to 1.0. The tube voltage was fixed at 120 kV, and the tube current (mA) was adjusted to give three CTDI$_{vol}$ values (table 3) as close as possible to the target values of 1.0, 3.2 and 10 mGy in order to have a range of ten in exposure. The detailed acquisition parameters are available in table 1.

The scans were performed in the same conditions for two different cylindrical phantoms, both centred at the scanner isocentre and aligned in the longitudinal direction using the positioning lasers. A first water phantom with a diameter of 25 cm and a length of 50 cm filled with water contained three central rods (8 cm diameter, 10 cm long) made of low-density polyethylene (PE, average CT number at 120 kVp ≈ -100 HU),

Table 1. Acquisition parameters.

System	Tube potential (kV)	Rotation time (s)	Current (fixed) (mA)	Pitch factor	Collimation (mm)	Diameter SFOV (mm)	SID (mm)	SDD (mm)	Al filtration (mm)
GE Discovery 750 HD	120	0.6	20/65/205	0.984	64 × 0.625	500	538.5	946.75	7.2
Siemens SOMATOM Force	120	0.5	30/96/300	1.000	48 × 1.2	500	595	1085.6	7.7

Table 2. Reconstruction parameters.

	Diameter DFOV (mm)	Pixel size (mm)	Kernel	Filter	Algorithm	Slice thickness (mm)	Slice interval (mm) Water phantom	Slice interval (mm) Catphan phantom
GE Discovery 750 HD	300	0.586	STD BONE	Body	FBP ASIR 50 ASIR-V 50	1.25/2.5/5.0	1.0/1.25/2.5	0.1
Siemens SOMATOM Force	300	0.586	Bf40f Br59f	Flat	FBP	1.5/3.0/5.0	0.75/1.5/2.5	0.1

Table 3. Dosimetry parameters.

System	$_nCTDI_{air}$ (mGy mAs^{-1})	$CTDI_{vol}$ (mGy)	P_{in} (μGy)	φ (mm^{-2} μGy^{-1})	μ_w (mm^{-1})	SF_{in}
GE Discovery 750 HD	0.2006	0.98/3.18/10.0	7.05/22.9/72.3	30 718	0.189	0.476
Siemens SOMATOM Force	0.2002	0.94/3.14/10.0	8.21/26.3/82.1	30 713	0.189	0.476

polymethylmethacrylate (PMMA or Plexiglas®, average CT number at 120 kVp ≈ 120 HU) and polytetrafluoroethylene (PTFE or Teflon®, average CT number at 120 kVp ≈ 1000 HU). These three materials simulate the densities of fat, soft tissues, and trabecular bone, respectively, and were used to compute the TTFs in the reconstructed transverse slices for the three materials (TTF_{xy}). The homogeneous volume of the water phantom was used to compute the NPS. Several scans of the water phantom were performed at each mA level to produce a sufficient signal-to-noise ratio for TTF_{xy} measurements: ten, five, and three scans for the target $CTDI_{vol}$ of 1, 3.2, and 10, respectively. The second phantom was the image quality Catphan® 600 phantom (The Phantom Laboratory, Greenwich, NY) with a diameter of 20 cm. Only the CTP 528 module of the Catphan was scanned to have the images of the point source (0.28 mm tungsten carbid bead) used for longitudinal TTF measurements (TTF_z).

All the data were reconstructed with the same pixel size of 0.586 mm (reconstructed FOV 300 mm—matrix 512 × 512) at three slice thicknesses: 1.25, 2.5, and 5.0 mm for the GE and 1.5, 3.0, and 5.0 mm for the Siemens. Reconstruction intervals equal to half the slice thicknesses were used for the water phantom, except for the 1.25 mm slices for the GE reconstructed every 1.0 mm. All the images of the Catphan module were oversampled using a 0.1 mm slice interval. The transverse slices were reconstructed using conventional filtered back-projection (FBP) for the two systems, and data acquired on the GE Discovery 750 HD were additionally reconstructed using adaptive statistical iterative reconstruction (IR) algorithms (ASIR and ASIR-V, both at a strength of 50%). The default Body and Flat reconstruction filters and the soft kernels Standard and Bf40f were used for the GE and Siemens, respectively. The data acquired at 3.2 mGy were additionally reconstructed using the sharp kernels Bone for the GE and Br59f for the Siemens. The detailed reconstruction parameters are available in table 2.

3.2. Dosimetry

The $CTDI_{air}$ was measured using a RaySafe X2 dosimeter (Unfors RaySafe AB, Billdal, Sweden) with a 100 mm-long pencil ionizing chamber (X2 CT sensor) positioned in air at the scanner's isocentre, centred in the x-ray beam collimation, at a distance of 50 cm beyond the end of the scanner couch. The chamber was scanned with a single rotation in the axial mode. The measured air kerma (K_{air}) was multiplied by the length

of the chamber (integration of K_{air} over 100 mm), and divided by the collimation width (L_c) and the tube load (product of the tube current I and rotation time t in mAs) to give the normalized $CTDI_{air}$ available in table 3 ($_nCTDI_{air}$).

$$_nCTDI_{air} = \frac{1}{L_c \cdot I \cdot t} \cdot \int\limits_{-50\,mm}^{+50\,mm} K_{air}\,dz \tag{12}$$

The $CTDI_{air}$ for the different acquisitions is the corresponding $_nCTDI_{air}$ multiplied by the effective tube load given by the tube current, rotation time and pitch factor (p).

$$CTDI_{air} = {}_nCTDI_{air} \cdot \frac{I \cdot t}{p} \tag{13}$$

The total x-ray beam filtration at the scanner isocentre in an equivalent aluminium thickness was measured with the same dosimeter in the same conditions. The effective energy of the x-ray beam and the fluence of photons per unit exposure at the system input (φ in equations (9) and (10) and in table 3) were calculated using the method described in Boone and Seibert (1997).

3.3. Scatter fraction at the system input (SF$_{in}$)

The scatter fraction (SF) at system input (SF_{in}) is used for the calculation of the system DQE. SF_{in} is the SF produced by the homogeneous water phantom for each projection at the projection point of the isocentre on the detector (image) plane, in the absence of an anti-scatter device. The configuration of CT systems does not allow a direct measurement of SF_{in}. This parameter was therefore measured on a radiography system that reproduces the geometry and effective energy of the scanners. The setup was similar to that used by Johns and Yaffe (1982), Siewerdsen and Jaffray (2001) or Endo *et al* (2006) for the measurement of SF_{in} for fan or cone beam geometry. The tube voltage, cone beam collimation at the isocentre (centre of the water phantom), SID and SDD of the CT scans were adjusted on the radiography system to mimic the SF produced by the water phantom in the CT systems. The additional aluminium filtration at the tube output was adapted to give the same total aluminium filtration measured at the isocentre of the scanners at 120 kV. We assumed that the differences in x-ray tube properties (e.g. target angle or shape of the bowtie filter) and off-focal radiations are negligible sources of variations on the SF. SF_{in} was measured using the beam stop method described in Monnin *et al* (2017). Lead blockers (14, 7, 5, 4 and 3 mm in diameter) were placed on top of the water phantom in the middle of the irradiated strip (collimation). 'For processing' images in a dicom format were acquired using a radiography flat planel detector (PaxScan 4336 W, Varian Medical Systems, Palo Alto, CA, U.S.). Unprocessed pixel values of the images were re-expressed in air kerma values using the measured response function of the system.

3.4. Task-based transfer functions (TTF)

A radial version of the angled edge method described in Samei *et al* (1998) was used for in-plane TTF measurements (TTF$_{xy}$). The edges of the cylindrical inserts of different densities in the water phantom gave the edge spread functions (ESF). A 10° angular aperture with a 5° angular pitch gave 72 radial ESFs calculated over 360° in square ROIs of 120×120 mm centred on the cylindrical inserts. Calculation steps from ESF to TTF are described in Monnin *et al* (2016). The 72 resulting radial pre-sampling TTFs were averaged to give the mean radial pre-sampling TTF$_{xy}$. For each condition, a TTF$_{xy}$ was measured for low-density PE (average CT number at 120 kVp ≈ -100 HU) and PMMA (average CT number at 120 kVp ≈ 120 HU) for soft kernels, and for PTFE (average CT number at 120 kVp ≈ 1000 HU) for sharp kernels.

For practical reasons, the longitudinal point spread functions (PSF$_z$) were measured for only one contrast from the point source of the Catphan phantom. The signal (HU) of the 0.28 mm bead was plotted for every slice as a function of the longitudinal position, giving the oversampling PSF$_z$. Because the bead is subpixel sized, no correction for the bead size was applied in the calculation. The longitudinal pre-sampling TTF$_z$ is the modulus of the Fourier transform of the PSF$_z$. A pre-sampling TTF$_z$ was measured for each scanner, dose level, slice thickness, kernel and reconstruction algorithm.

3.5. Noise power spectra (NPS)

Three dimensional NPS were measured from homogeneous volumes of interest (VOIs) of $150 \times 150 \times 50$ mm placed at the centre of the homogeneous volume of water in the cylindrical water phantom. 3D NPS of a given VOI are the magnitude squared of the 3D Fourier Transform of each VOI, calculated using equation (14).

$$NPS(f_x, f_y, f_z) = \frac{\Delta x \cdot \Delta y \cdot \Delta z}{N_x \cdot N_y \cdot N_z} \left| \iiint \left(d(x,y,z) - \bar{d} \right) \cdot \exp\left(-i2\pi \left(f_x x + f_y y + f_z z \right)\right) dx\,dy\,dz \right|^2 \tag{14}$$
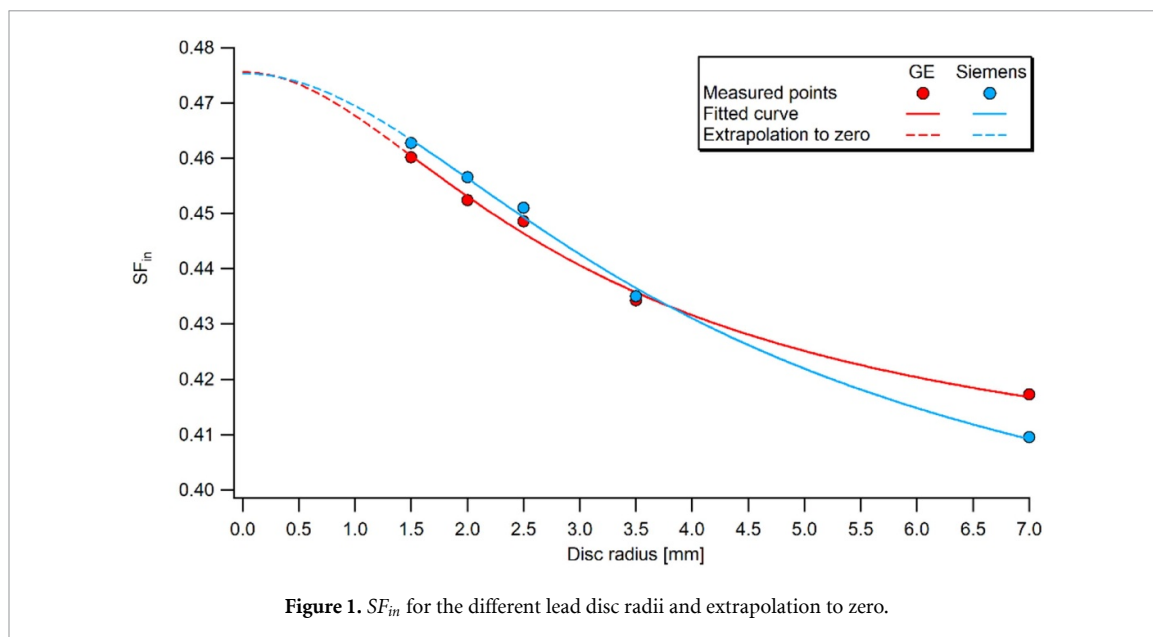
Figure 1. SF_{in} for the different lead disc radii and extrapolation to zero.

Where, $d(x,y,z)$ is the pixel value at the position (x,y,z), $\bar{d}$ is the mean pixel value in the VOI, N_x, N_y, N_z and Δx, Δy, Δz are the number of voxels and voxel spacing in the x-, y- and z-directions, respectively. The unit of the 3D NPS measured on the CT images is HU^2 mm^3. The 3D NPS for each mAs are averages of the ten, five, and three scans for the target $CTDI_{vol}$ of 1.0, 3.2, and 10 mGy, respectively. No detrending correction was applied to subtract large inhomogeneities from the VOIs before noise analysis. The synthesized (in-plane) 2D NPS_{xy} were obtained by integrating the 3D NPS along the z-axis, as defined by Siewerdsen *et al* (2002). The 1D NPS curves are radial averages of the 2D NPS_{xy}, excluding the 0° and 90° axial values. The unit of the 1D NPS is HU^2 mm^2.

4. Results and discussion

4.1. Dosimetry and input scatter fraction
The measured $CTDI_{air}$ were 0.2006 and 0.2055 mGy mAs^{-1} for the GE and Siemens scanners, respectively, close to the values given by the manufacturers (0.2003 and 0.198 mGy mAs^{-1} for the GE and Siemens). The equivalent aluminium filtrations measured at the scanners isocentre were 7.2 and 7.7 mm, which agreed with the manufacturer-provided values, 7.3 mm for the GE and 7.8 mm for the Siemens. The corresponding effective energies were 73.9 keV and 74.1 keV, and gave a linear attenuation coefficient for water $\mu_w = 0.189$ cm^{-1}. The calculated fluence of photons at the output of the water phantom was 30 718 and 30 713 photons mm^{-2} μGy^{-1} for the GE and Siemens, respectively.

The scatter fraction measured at the system input (SF_{in}) was 0.476 for the two scanners. The fitted curve and the extrapolation to zero that gives SF_{in} are shown in figure 1. Details of the calculation can be seen in Monnin *et al* (2017). The larger collimation of the Siemens (57.6 × 300 mm against 40 × 300 mm for the GE) produced a higher scatter fraction at the object output. However, the larger object-to-detector distance for the Siemens (491 mm against 408 mm for the GE) reduced the SF at the detector and compensated for the higher SF produced in the phantom. The difference in 0.5 mm Al filtration between the two scanners did not give a measurable difference in SF_{in}, mostly determined by the water thickness, SID/SDD ratio and collimation width. The levels of influence of these parameters on SF_{in} agree with those found in Johns and Yaffe (1982). It is of note this measurement only gives SF_{in} in one point, at the projection of the isocentre on the detector. The detailed dosimetric parameters are available in table 3.

4.2. Spatial resolution
The in-plane spatial resolution is largely determined by the reconstruction kernel for both scanners, with cut-off frequencies at 0.8 mm^{-1} for the Standard and Bf40f kernels, 1.2 mm^{-1} for the Br59f kernel, and 1.4 mm^{-1} for the Bone kernel (figure 2). The TTF_{xy} shape differs between the two scanners, e.g. the Br59f filter of the Siemens enhances spatial frequencies until 0.5 mm^{-1} whereas the Bone filter of the GE does not. In-plane resolution does not depend on the contrast and the dose for FBP, but may depend for IR. This is characteristic for non-linear algorithms for which contrast and dose may influence the resolution. The TTF_{xy} increases with the contrast for ASIR and ASIR-V. Compared to FBP, ASIR and ASIR-V give lower in-plane
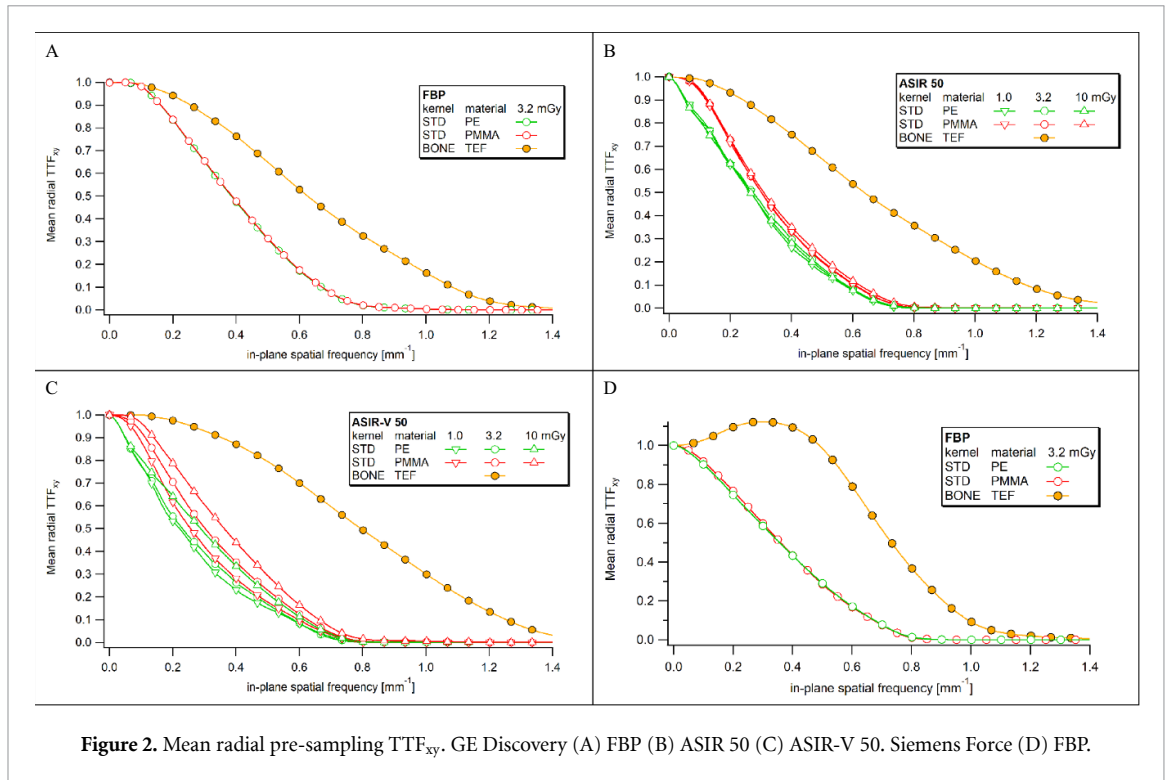
Figure 2. Mean radial pre-sampling TTF$_{xy}$. GE Discovery (A) FBP (B) ASIR 50 (C) ASIR-V 50. Siemens Force (D) FBP.
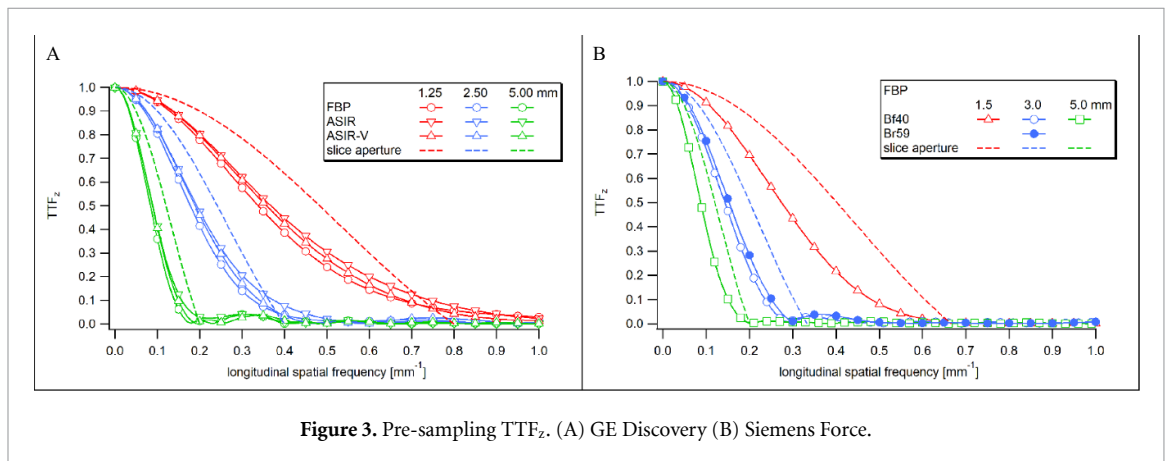

Figure 3. Pre-sampling TTF$_z$. (A) GE Discovery (B) Siemens Force.

resolution than FBP for the PE modulus but higher for PMMA and Teflon ones. An increase in spatial resolution as a function of the dose was observed for ASIR-V, but not for ASIR. TTF$_{xy}$ of this study are consistent with those obtained for the standard kernel using FBP, ASIR 40, and ASIR 50 on GE Discovery scanners (Richard *et al* 2012, Ott *et al* 2014) and using ASIR-V on a GE Revolution scanner (Rotzinger *et al* 2018, Greffier *et al* 2020).

The TTF$_z$ measured using the Catphan phantom bead were all close to their theoretical maximal values given by the slice apertures (dotted lines in figure 3). The reconstruction algorithms played only a marginal role on TTF$_z$, and no difference could be measured for the three dose levels (1.0, 3.2 and 10 mGy) and between the Standard and Bone kernels for the GE (data not shown). The slice thickness is thus the main parameter that determines the pre-sampling TTF$_z$. TTF$_{xy}$ remains constant under varying slice thicknesses, and TTF$_z$ does not change significantly under varying reconstruction algorithms or kernels. This confirms that TTF$_{xy}$ and TTF$_z$ can be measured independently, and supports equation (4*b*) is a valuable expression for the slice NEQ.

4.3. Noise power spectra (NPS)

As expected, the in-plane synthesized NPS is roughly inversely proportional to the CTDI$_{vol}$ and to the slice thickness, regardless the reconstruction algorithm (figure 4). The NPS curves reach their maximal intensity around 0.15 mm^{-1} and 0.25 mm^{-1} for the soft kernels Standard and Bf40f, and around 0.60 mm^{-1} and 0.85 mm^{-1} for the sharp kernels Bone and Br59f. The various kernels demonstrate different trade-offs

Figure 4. Mean radial NPS. GE Discovery (A) FBP (B) ASIR 50 (C) ASIR-V 50. Siemens Force (D) FBP.
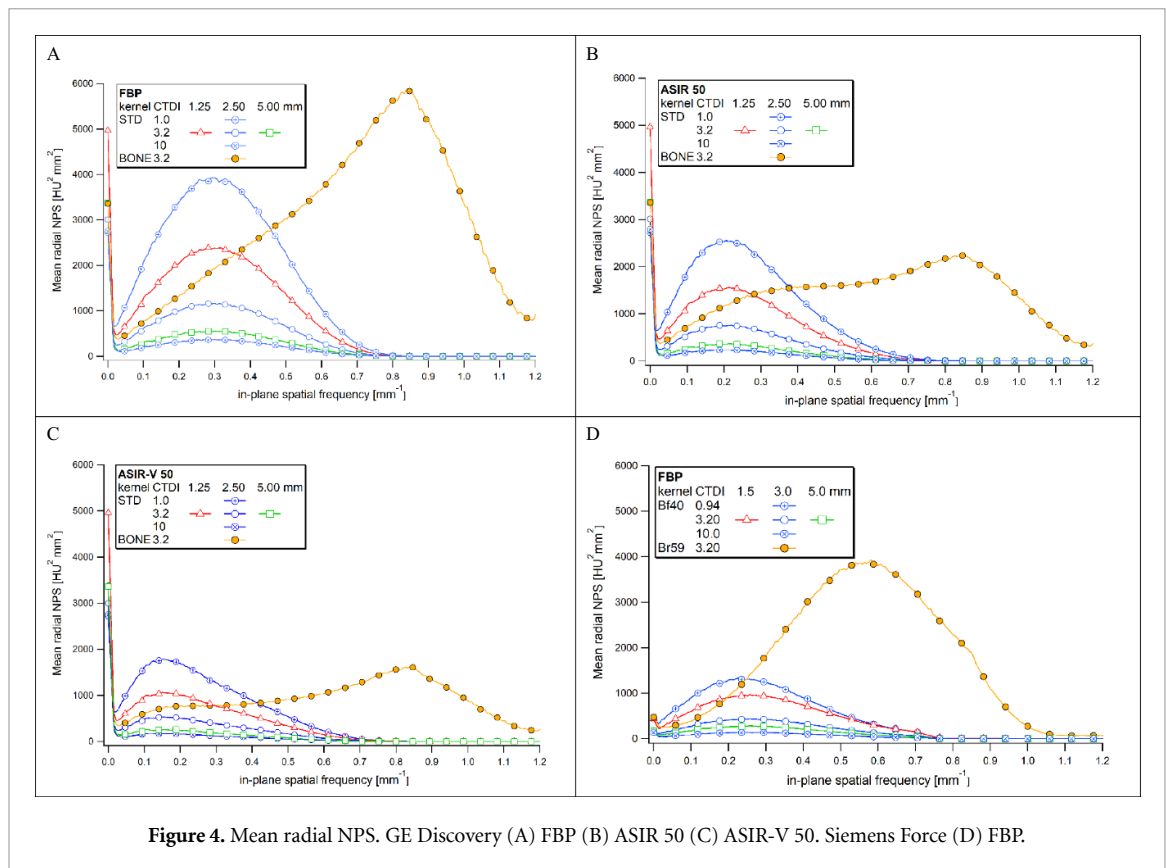
between spatial resolution and image noise. The soft kernels pass only low-frequency noise whereas sharp kernels give a better spatial resolution but more high-frequency noise. The positive slope at low frequency results from the ramp filter used in FBP, and the negative slope at higher spatial frequencies is due to the roll-off properties of the reconstruction kernel and filter used to dampen high-frequency noise in the images. The NPS spikes below 0.01 mm^{-1} come from low-frequency trends of HU in the images, in which HU values in the homogeneous water phantom tend to increase from the centre to the periphery. This artefact comes typically from beam hardening or scattered radiation. Techniques of detrending can be used to subtract away these large inhomogeneities before noise analysis (Dobbins *et al* 2006), but no correction was applied in this study.

4.4. Noise equivalent quanta (NEQ)

The 2D NEQ (figure 5) and slice NEQ (figure 6) are inversely proportional to the NPS, and are therefore proportional to CTDI$_{vol}$. The ratio between TTF^2 and NPS mitigates the influence of the kernel in the NEQ for FBP reconstructions, but not for ASIR and ASIR-V. IR introduce different spatial correlations between pixels for signal and noise (edge enhancement and noise smoothing), and hence decorrelate the NPS from the TTF^2. IR give therefore higher NEQ at high spatial frequency compared to FBP reconstructions.

The 2D NEQ (equation (2)) increases linearly with the slice thickness as the number of photons does in a slice for a given CTDI$_{vol}$ (figure 5). This behaviour would make sense if the NEQ described the frequency-dependent signal-to-noise ratio visible on the reconstructed images as it does in projection radiography. Filtered backprojection used in CT decorrelates signal and noise. Consequently, the NEQ in CT does not represent a signal-to-noise ratio, but gives the number of photons per unit length of projection (for all the projections) that a perfect system would need to give the NPS observed on the images. The 2D NEQ usually used in CT does not consider the slice thickness and gives a number of photons summed over the longitudinal length, with unit photons/mm. Decreasing the longitudinal resolution increases the correlation between pixels and reduces the longitudinal frequency bandwidth. The NPS measured in a slice integrates all longitudinal frequencies (Siewerdsen *et al* 2002) and any decrease in longitudinal resolution will decrease the NPS and incorrectly inflate the NEQ. This means that 2D NEQ cannot be used to compare imaging performance between two scanners when different slice thicknesses or different longitudinal resolutions are used. Hence, the 2D NEQ represents neither a signal-to-noise ratio in the CT slice nor a performance of the scanner in terms of image quality.

Figure 5. Mean radial 2D NEQ. GE Discovery (A) FBP (B) ASIR 50 (C) ASIR-V 50. Siemens Force (D) FBP.
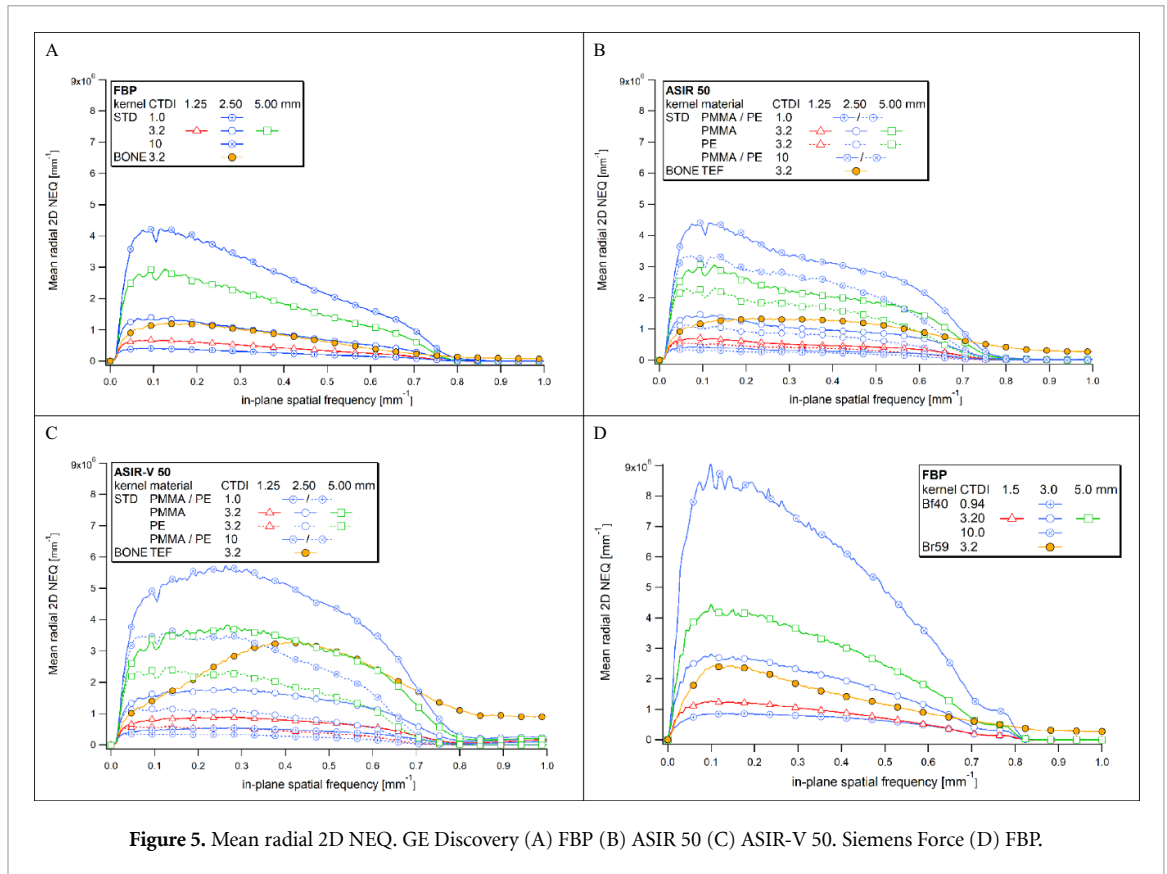
The 2D NEQ (equation (2)) and slice NEQ (equation (4b)) have the same frequency content (same shape) because they differ only in the value of the bandwidth integral of $TTF_z^2 (f_z)$, with unit mm^{-1}. They have therefore different units, mm^{-1} for the 2D NEQ against mm^{-2} for the slice NEQ, and their level differs as a function of the longitudinal information bandwidth integral (IBWI) as defined by Wagner *et al* (1979). The slice NEQ mitigates the influence of the slice thickness to give the real equivalent number of photons an ideal scanner would have used to give the observed NPS for the chosen slice thickness. It provides a volumetric indication of the scanner imaging performance, and makes it possible to compare the imaging performance between images reconstructed with different slice thicknesses or between scanners with different performances in longitudinal resolution. The slice NEQ peaks at 2.10^5 and 3.10^5 mm^{-2} at 3.2 mGy for FBP for the GE and Siemens, respectively, and indicates the Force system has a higher volumetric imaging performance than the Discovery.

IR introduced differences in NEQ for the different materials, giving contrast-dependent NEQ. The slice NEQ showed small variations between PE and PMMA for ASIR and ASIR-V when using different slice thicknesses (figures 6(A) and 6(C)), whereas it remained constant with slice thickness for FBP (figure 6(A)). The importance of this effect increases with the degree of nonlinearity of the reconstruction algorithm. Based on this observation, ASIR and ASIR-V show a low and high degree of nonlinearity. The degree of nonlinearity of IR can be primarily estimated by measuring the variations of TTF$_{xy}$ and TTF$_z$ as a function of dose and contrast. In this study, the global agreement of the slice NEQ for the different materials indicates that the results yield a good approximation to real imaging performance for IR with small nonlinearities. We therefore expect small differences between TTF$_z$ for the low contrast PE and PMMA and those measured at high contrast using the Catphan bead for ASIR and ASIR-V. The metrics proposed in this study produced valuable information on the behaviour of FBP, ASIR and ASIR-V, but TTF$_{xy}$ and TTF$_z$ should in principle be measured using the same task-based contrasts for nonlinear IR. Nevertheless, to our knowledge, an accurate measurement method of TTF$_z$ with low-CNR conditions has not yet been validated. This is a limitation for an accurate characterization and optimization of CT and CBCT imaging performance with nonlinear IR under low CNR conditions.

4.5. System DQE
The system DQE is an efficiency index for the whole imaging system composed of the anti-scatter device, detector, and reconstruction algorithm. DQE$_{sys}$ for the Siemens Force peaks at 0.70 around 0.1 mm^{-1} against 0.50 around 0.1 mm^{-1} for the GE Discovery for FBP reconstructions (figures 7(A) and 7(D)). ASIR 50 and
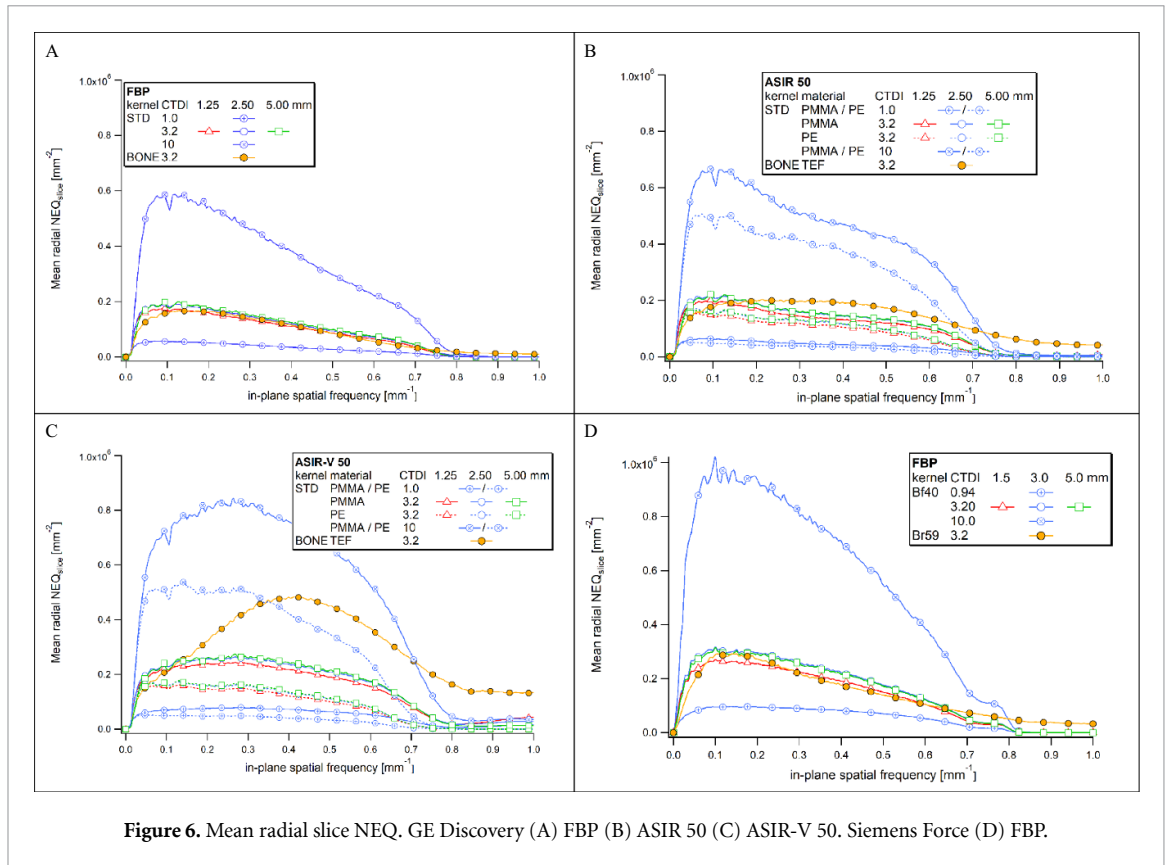
Figure 6. Mean radial slice NEQ. GE Discovery (A) FBP (B) ASIR 50 (C) ASIR-V 50. Siemens Force (D) FBP.

ASIR-V 50 give a higher DQE_{sys} than FBP for the PMMA and Teflon but lower for the PE (figures 7(B) and 7(C)). For IR, DQE_{sys} increases with the material contrast. For linear and shift invariant systems, DQE_{sys} is independent of the contrast, kernel, and reconstruction algorithm. It is furthermore independent of the dose for quantum limited systems. FBP reconstructions roughly met these requirements in our study. For IR, the contrast and dose can influence the reconstruction parameters and finally the system DQE. This effect is particularly visible for the high contrasted Teflon that gave a DQE higher than 1.0 for ASIR-V within a frequency range between 0.25 and 0.55 mm^{-1}. This shows how efficiently this algorithm decorrelates the signal and the noise.

As discussed for the NEQ, be careful when interpreting the DQE_{sys} because Fourier metrics require linear processes and shift invariance that are clearly not fully satisfied for high contrasted materials with IR. This means that the system DQE proposed in this study should only be used for FBP reconstructions and only within a small range of low contrasted materials for IR. The exact extent to which nonlinear effects in CT degrade the DQE still needs to be explored in future works. The validity of DQE_{sys} is furthermore restricted to the vicinity of the isocentre of the system where the TTF, NPS, and CTDI$_{air}$ were measured.

In the conditions specified above, we propose DQE_{sys} as an alternative to the standard DQE for evaluating the overall imaging efficiency of CT systems. The standard DQE measured in air is not practicable in CT as a cylindrical object is needed for measuring the resolution and noise, and the DQE proposed by Hanson (1979) and Wagner *et al* (1979) are difficult to calculate. The bowtie filter and the cylindrical water phantom modulate the photon fluence in the field of view and necessitate a numerical integration over the phantom section. Our system DQE is based on the standardized measure of the CTDI$_{air}$ and sidesteps these difficulties but requires an additional measurement of the scatter fraction at the system input (SF_{in}). SF_{in} is essentially determined by the diameter of the water phantom used for the measurement, and standardized values of SF_{in} could be envisaged for routine use of DQE_{sys} in CT.

4.6. Limitations of the metrics

Compared to 2D NEQ, the assessment of slice NEQ needs to additionally measure longitudinal resolution (TTF$_z$). Beads, edges or wires of high contrast are commonly used to produce an impulse response with a sufficient contrast-to-noise ratio (CNR) for an accurate measurement (Greene and Rong 2014, Cruz-Bastida *et al* 2016, Robins *et al* 2018, Tominaga *et al* 2018). The resolution of linear systems does not depend on the amplitude of signal and noise. High contrast objects can assess the resolution for FBP reconstructions. However, nonlinear IR can produce images in which resolution is contrast and noise (dose) dependent. An
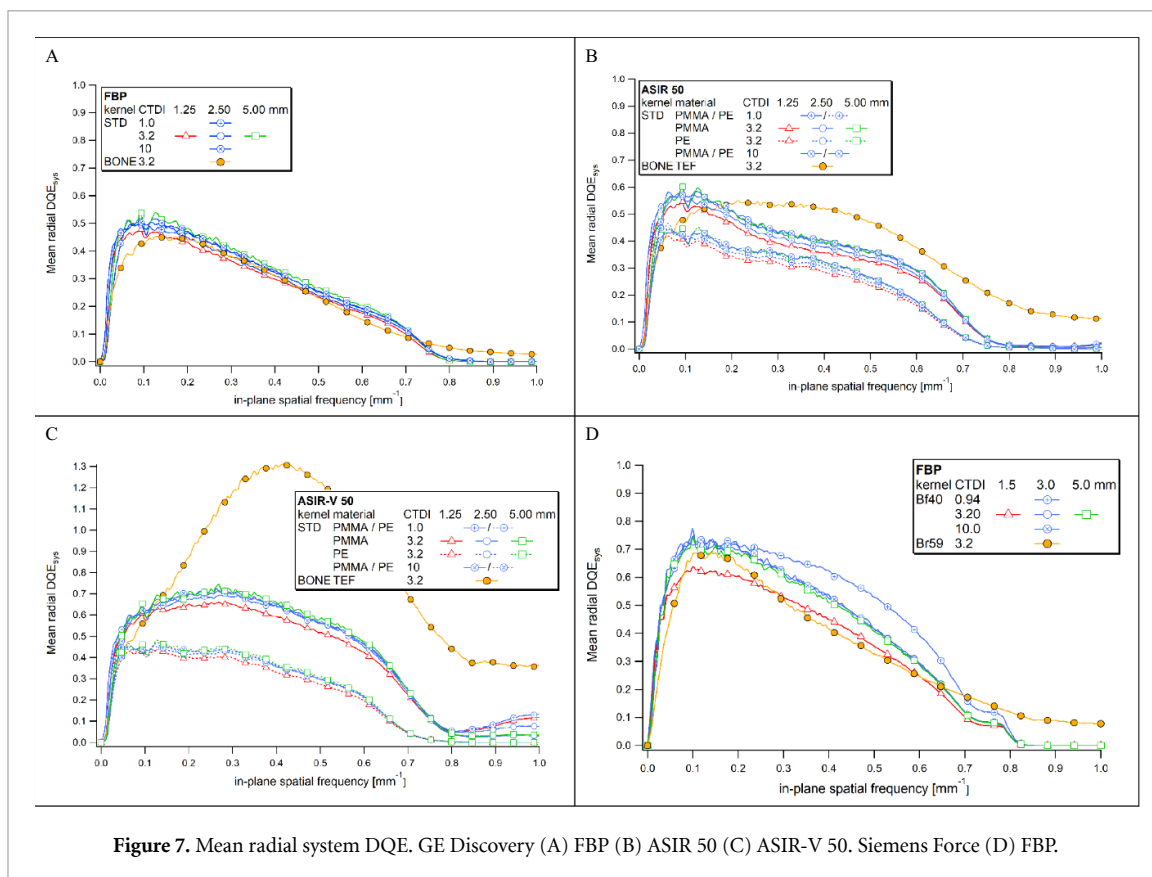
Figure 7. Mean radial system DQE. GE Discovery (A) FBP (B) ASIR 50 (C) ASIR-V 50. Siemens Force (D) FBP.

analysis of imaging performance with transfer functions is a linear approximation to a nonlinear system and must be assessed under task-based conditions for IR, using the hypothesis of small signal system linearity. A small signal model accounts for the system behavior which is linear around an operating point (dose and contrast). In this study, TTF_{xy} were measured for three different contrasts and doses, giving nine CNR levels, whereas TTF_z were measured with one contrast and three dose levels. Recent studies have shown small changes in longitudinal resolution with object contrast or with CNR for IR, as a function of the reconstruction algorithm and its strength (Li *et al* 2014, Tominaga *et al* 2018, Goto *et al* 2019). The edges of the three rods of our phantom could have been used for the assessment of TTF_z for the three contrasts. However, the number of scans needed to produce an acceptable accuracy in the measured PSF_z was extremely high and not practically feasible. Furthermore, with this method, the differentiation of the edge profile worsens noise, only one image per scan can be used for TTF_z measurement and cone-beam artifacts at the edges can produce variations in longitudinal PSF_z with the longitudinal phase of the object according to helical scan orbit (Goto *et al* 2019). An accurate method of measurement of PSF_z at low-CNR condition has not been fully established yet and is still a field of research.

The 0.28 mm point source of the Catphan phantom gave peak contrasts around 800, 500 and 300 HU for the 1.25, 2.5 and 5 mm slice thicknesses, respectively. These values find themselves within the contrast range of the task-based Teflon (1000 HU), PMMA (120 HU) and PE (100 HU) materials used in this study. The three dose levels did not give measurable differences in TTF_z for the contrasts produced by the bead of the Catphan phantom. However, this result cannot be extrapolated for low contrasts. Tominaga *et al* (2018) and Goto *et al* (2019) showed that the PSF_z for ASIR and ASIR-V was CNR-dependent with variations around peak CNR thresholds between 10 and 50 for ASIR and between 2 and 5 for ASIR-V. Slice NEQ slightly increased with contrast for ASIR or ASIR-V. However, the small variations of the slice NEQ between PMMA and PE (figures 6(B) and 6(C)) indicate that the slice NEQ gave coherent and robust results for these two materials. For this reason, the variation in TTF_z with contrast is expected to remain small. This implies that with the CNR conditions used in this study, TTF_z measured at a fixed contrast are accurate. In a general way, it is important to remember that linearity and shift-invariance of resolution and noise in the image plane are only approximations, and Fourier-based metrics make a linear approximation that simplifies the analysis of the real imaging performance of CT systems and can be used as long as the results give a good approximation to reality. If test objects give a high signal not compatible with the assumption of linearity, a statistical analysis performed in the spatial domain will be more appropriate for the assessment of CT imaging performance.

Compared to the slice NEQ, the system DQE needs a measurement of SF_{in} that is not directly possible on CT systems because of the need of projection images acquired without an anti-scatter device. SF_{in} assessment using the beam blocker method needed additional measurements using a digital radiography system that mimics the cone beam geometry and beam quality of the scanners. The main influencing parameters (phantom, beam collimation, distances, tube potential and effective energy) were properly reported on the radiography system. Using different equipment can lead to some variations in scatter radiations produced by the tube itself and off-focal radiations. The influence of these radiations on the SF produced within the phantom and on SF_{in} measured on the detector remains very low (fan beam and long source-to-detector distance) but still constitutes an intrinsic limitation of the metrics.

5. Conclusion

This work introduced and tested the slice NEQ and system DQE for assessing the image quality and imaging efficiency of CT scanners considering the entire imaging system of anti-scatter device, detector, and algorithm reconstruction. The slice NEQ is invariant with the slice thickness and enables a comparison of the imaging performance between images reconstructed with different slice thicknesses or between scanners with different longitudinal resolutions. Compared to 2D NEQ, the slice NEQ needs the measure of the pre-sampling longitudinal TTF but gives in return a suitable metric for optimising 3D imaging systems, including the impact of the longitudinal resolution and noise on image quality in the reconstructed slice. The system DQE formulation proposes an efficiency index measured at the isocentre that can be used for CT benchmarking and quality control protocols.

References

Boedeker K L, Cooper V N and Mcnitt-Gray M F 2007 Application of the noise power spectrum in modern diagnostic MDCT: part I. Measurement of noise power spectra and noise equivalent quanta *Phys. Med. Biol.* **52** 4027

Boone J M and Seibert A 1997 An accurate method for computer-generating tungsten anode x-ray spectra from 30 to 140 kV *Med. Phys.* **24** 1661–70

Brunner C C and Kyprianou I S 2013 Material-specific transfer function model and SNR in CT *Phys. Med. Biol.* **58** 7447

Cruz-Bastida J P, Gomez-Cardona D, Li K, Sun H, Hsieh J, Szczykutowicz T P and Chen G H 2016 Hi-Res scan mode in clinical MDCT systems: experimental assessment of spatial resolution performance *Med. Phys.* **43** 2399–409

Dobbins J T, Samei E, Ranger N T and Chen Y 2006 Intercomparison of methods for image quality characterization. II. Noise power spectrum *Med. Phys.* **33** 1466–75

Endo M, Mori S, Tsunoo T and Miyazaki H 2006 Magnitude and effects of x-ray scatter in a 256-slice CT scanner *Med. Phys.* **33** 3359–68

Faulkner F and Moores B M 1984 Analysis of x-ray computed tomography images using the noise power spectrum and autocorrelation function *Phys. Med. Biol.* **29** 1343

Gang G J, Lee J, Stayman J W, Tward D J, Zbijewski W, Prince J L and Siewerdsen J H 2011 Analysis of Fourier-domain taks-based detectability index in tomosynthesis and cone-beam CT in relation to human observer performance *Med. Phys.* **38** 1754–68

Gang G J, Stayman J W, Zbijewski W and Siewerdsen J H 2014 Task-based detectability in CT image reconstruction by filtered backprojection and penalized likelihood estimation *Med. Phys.* **41** 081902-1-19

Goto M, Tominaga C, Taura M, Azumi H, Sato K, Homma N and Mori I 2019 A method to measure slice sensitivity profiles of CT images under low-contrast and high-noise conditions *Phys. Med.* **60** 100–10

Greene T C and Rong X J 2014 Evaluation of techniques for slice sensitivity profile measurement and analysis *JACMP* **15** 281–94

Greffier J, Frandon J, Larbi A, Beregi J P and Pereira F 2020 CT iterative reconstruction algorithms: a task-based image quality assessment *Eur. Radiol.* **30** 487–500

Hanson K M 1979 Detectability in computed tomographic images *Med. Phys.* **6** 441–51

ICRU Report 54 1996 *Medical imaging—The assessment of image quality.* J ICRU os 28. (10.1093/jicru/os28.1.Report54).

Johns P C and Yaffe M 1982 Scattered radiation in fan beam imaging systems *Phys. Med.* **9** 231–9

Li K, Garrett J, Ge Y and Chen G H 2014 Statistical model based iterative reconstruction (MBIR) in clinical CT systems. Part II. Experimental assessment of spatial resolution performance *Med. Phys.* **41** 071911

Monnin P, Bosmans H, Verdun F R and Marshall N W 2016 A comprehensive model for quantum noise characterization in digital mammography *Phys. Med. Biol.* **61** 2083

Monnin P, Verdun F R, Bosmans H, Rodriguez Pérez S and Marshall N W 2017 A comprehensive model for x-ray projection imaging system efficiency and image quality characterization in the presence of scattered radiations *Phys. Med. Biol.* **62** 5691

Ott J G, Becce F, Monnin P, Schmidt S, Bochud F O and Verdun F R 2014 Update of the non-prewhitening model observer in computed tomography for the assessment of the adaptive statistical and model-based iterative reconstruction algorithms *Phys. Med. Biol.* **59** 4047

Richard S, Husarik D B, Yadava G, Murphy S N and Samei E 2012 Towards task-based assessment of CT performance: system and object MTF across different reconstruction algorithms *Med. Phys.* **39** 4115–22

Robins M, Salomon J, Richards T and Samei E 2018 3D task-transfer function representation of the signal transfer properties of low-contrast lesions in FBP- and iterative-reconstructed CT *Med. Phys.* **45** 4977–85

Rotzinger D C, Racine D, Beigelman-Aubry C, Alfudhili K M, Keller N, Monnin P, Verdun F R and Becce F 2018 Task-based model observer assessment of a partial model-based iterative reconstruction algorithm in thoracic oncologic multidetector CT *Sci. Rep.* **8** 1–12

Samei E *et al* 2019 Performance evaluation of computed tomography systems: summary of AAPM Task Group 233 *Med. Phys.* **46** e735–56

Samei E, Flynn M J and Reimann D A 1998 A method for measuring the presampled MTF in digital radiographic systems using an edge test device *Med. Phys.* **25** 102–13

Siewerdsen J H, Cunningham I A and Jaffray D A 2002 A framework for noise-power spectrum of multi-dimensional images *Med. Phys.* **29** 2655–71

Siewerdsen J H and Jaffray D A 2001 Cone-beam computed tomography with a flat panel imager: magnitude and effects of x-ray scatter *Med. Phys.* **28** 220–31

Siewerdsen J H and Jaffray D A 2003 Three-dimensional NEQ transfer characteristics of volume CT using direct and indirect-detection flat-panel imagers *Proc. SPIE* **5030** 92–102

Tang X, Yang Y and Tang S 2012 Imaging performance in differential phase contrast CT comparted with the conventional CT-Noise equivalent quanta NEQ(k) *Proc. SPIE* **8313** 83132I

Tominaga C, Azumi H, Goto M, Taura M, Homma N and Mori I 2018 Tilted-wire method for measuring resolution properties of CT images under extremely low-contrast and high-noise conditions *Radiol. Phys. Technol.* **11** 125–37

Tward D J and Siewerdsen J H 2008 Cascaded systems analysis of the 3D noise transfer characteristics of flat-panel cone-beam CT *Med. Phys.* **35** 5510–29

Tward D J, Siewerdsen J H, Fahrig R A and Pineda A R 2008 Cascaded systems analysis of the 3D NEQ for cone-beam CT and tomosynthesis *Proc. SPIE* **6913** 6913S

Vaishnav J Y, Jung W C, Popescu L M, Zeng R and Myers K J 2014 Objective assessment of image quality and dose reduction in iterative CT reconstruction *Med. Phys.* **41** 071904-1-12

Verdun F R *et al* 2015 Image quality in CT: from physical measurements to model observers *Phys. Med.* **31** 823–43

Wagner R F and Brown D G 1985 Unified SNR analysis of medical imaging systems *Phys. Med. Biol.* **30** 489

Wagner R F, Brown D G and Pastel M S 1979 Application of information theory to the assessment of computed tomography *Med. Phys.* **6** 83–94

Willemink M J, Leiner T, de Jong P A, de Heer L M, Nievelstein R A, Schilham A M and Budde R P 2013 Iterative reconstruction techniques for computed tomography part 2: initial results in dose reduction and image quality *Eur. Radiol.* **23** 1632–42